Measurement of the evolution of a plasma column by modulation of a high-energy proton beam

S. Gessner,[1] E. Adli,[2] A. Ahuja,[1] O. Apsimon,[3,4] R. Apsimon,[5,4] A.-M. Bachmann,[1,6,7] F. Batsch,[1,6,7] C. Bracco,[1] F. Braunmüller,[6] S. Burger,[1] G. Burt,[5,4] B. Buttenschön,[8] A. Caldwell,[6] J. Chappell,[9] E. Chevallay,[1] M. Chung,[10] D. Cooke,[9] H. Damerau,[1] G. Demeter,[11] L.H. Deubner,[12] A. Dexter,[5,4] S. Doebert,[1] J. Farmer,[13] V.N. Fedosseev,[1] R. Fiorito,[14,4] R.A. Fonseca,[15] F. Friebel,[1] L. Garolfi,[1] B. Goddard,[1] I. Gorgisyan,[1] A.A. Gorn,[16,17] E. Granados,[1] O. Grulke,[8,18] E. Gschwendtner,[1] A. Hartin,[9] A. Helm,[19] J.R. Henderson,[5,4] M. Hüther,[6] M. Ibison,[14,4] S. Jolly,[9] F. Keeble,[9] M.D. Kelisani,[1] S.-Y. Kim,[10] F. Kraus,[12] M. Krupa,[1] T. Lefevre,[1] Y. Li,[3,4] S. Liu,[20] N. Lopes,[19] K.V. Lotov,[16,17] M. Martyanov,[6] S. Mazzoni,[1] V.A. Minakov,[16,17] J.C. Molendijk,[1] J.T. Moody,[6] M. Moreira,[19,1] P. Muggli,[6,1] H. Panuganti,[1] A. Pardons,[1] F. Peña Asmus,[6,7] A. Perera,[14,4] A. Petrenko,[1,16] A. Pukhov,[13] S. Rey,[1] P. Sherwood,[9] L.O. Silva,[19] A.P. Sosedkin,[16,17] P.V. Tuev,[16,17] M. Turner,[1] F. Velotti,[1] L. Verra,[1,21] V.A. Verzilov,[20] J. Vieira,[19] C.P. Welsch,[14,4] M. Wendt,[1] B. Williamson,[3,4] M. Wing,[9] B. Woolley,[1] and G. Xia[3,4]

(The AWAKE Collaboration)

[1] *CERN, Geneva, Switzerland*

[2] *University of Oslo, Oslo, Norway*

[3] *University of Manchester, Manchester, UK*

[4] *Cockcroft Institute, Daresbury, UK*

[5] *Lancaster University, Lancaster, UK*

[6] *Max Planck Institute for Physics, Munich, Germany*

[7] *Technical University Munich, Munich, Germany*

[8] *Max Planck Institute for Plasma Physics, Greifswald, Germany*

[9] *UCL, London, UK*

[10] *UNIST, Ulsan, Republic of Korea*

[11] *Wigner Research Center for Physics, Budapest, Hungary*

[12] *Philipps-Universität Marburg, Marburg, Germany*

[13] *Heinrich-Heine-University of Düsseldorf, Düsseldorf, Germany*
[14] *University of Liverpool, Liverpool, UK*
[15] *ISCTE - Instituto Universitéario de Lisboa, Portugal*
[16] *Budker Institute of Nuclear Physics SB RAS, Novosibirsk, Russia*
[17] *Novosibirsk State University, Novosibirsk, Russia*
[18] *Technical University of Denmark, Lyngby, Denmark*
[19] *GoLP/Instituto de Plasmas e Fusão Nuclear,*
Instituto Superior Técnico, Universidade de Lisboa, Lisbon, Portugal
[20] *TRIUMF, Vancouver, Canada*
[21] *University of Milan, Milan, Italy*
(Dated: June 1, 2019)

Abstract

The AWAKE experiment at CERN is a proof-of-concept proton beam-driven plasma wakefield accelerator. The plasma source is a 10 meter-long Rubidium vapor cell ionized by a high-intensity laser pulse. The proton beam is modulated by the plasma, which results in micro-bunching at the plasma frequency and resonant excitation of the plasma wave. The modulation process is sensitive to the relative timing of the laser pulse with respect to the proton beam. We measure the frequency of the micro-bunching when the laser and proton beams are coincident, and when the proton beam propagates through the plasma long after the passage of the laser pulse. The plasma density is inferred from the frequency of modulation of the proton beam. We observe a microsecond-long plateau in the plasma density, followed by a power-law decay of the density versus time. Finally, we discuss the implications of this measurement for high-repetition rate plasma wakefield accelerators based on the seeded self-modulation concept.

I. INTRODUCTION

The Advanced Wakefield Experiment (AWAKE) at CERN is the first plasma wakefield acceleration (PWFA) experiment to use a high-energy proton beam driver [1–4]. The 400 GeV proton beam from the Super Proton Synchrotron (SPS) accelerator contains approximately 3×10^{11} particles per bunch, and the total stored energy in the beam is nearly 20 kJ, three orders of magnitude greater than the energy of electron beam drivers [5] and laser pulse drivers [6] used in state-of-art plasma acceleration experiments. The large amount of energy stored in the proton beam has the potential to simplify the design of a plasma wakefield accelerator: a trailing beam of electrons can be accelerated to extremely high energies in a single plasma stage, eliminating the need for complicated staging mechanisms [7–9].

While the SPS proton bunch delivers an unprecedented amount of energy for a PWFA experiment, it also poses a novel challenge in that the bunch length σ_z is much longer than the plasma wavelength λ_p. In typical PWFA experiments, the drive bunch is shorter than the plasma wavelength and can drive a high-amplitude wakefield as soon as it enters the plasma, but the proton beam at AWAKE is too long to effectively couple to the plasma wave. However, the proton beam excites a self-modulation instability (SMI) as it passes through the plasma, which causes the beam to form micro-bunches separated by the plasma wavelength [10–12]. The micro-bunches act together to resonantly drive a high-amplitude wakefield.

In order to control the onset of SMI, we use a high-power laser pulse to seed the instability. This process is referred to as seeded self-modulation (SSM) [13]. The seed pulse passes through and ionizes a rubidium (Rb) vapor source coincident with the passage of the proton beam. The seed pulse is temporally centered within the proton beam, such that the head of the beam transits through vapor and the tail transits through plasma. As the SSM develops, the micro-bunches and the plasma wave that they excite have a fixed phase with respect to the seed pulse. The SSM phenomenon was recently demonstrated in a series of experiments at AWAKE [14, 15].

The onset of micro-bunching is sensitive to the timing of the laser pulse with respect to the proton beam. If there is ionization of the Rb vapor ahead of the seed pulse, for instance caused by a laser pre-pulse or residual plasma from the previous shot, the head of the proton beam will also travel through plasma and excite a wake with a random phase with respect

to the seed pulse. This wake competes with the wake created through the SSM process and should be suppressed. In addition, a deleterious transverse hose instability may arise in the case of un-seeded SMI [16]. It is therefore important to understand the degree to which a pre-ionized plasma affects the proton beam and how long the plasma persists after ionization, as this will influence the repetition rate of a plasma accelerator based on the SSM mechanism.

In this work, we report on the lifetime and evolution of the plasma channel by inferring the plasma density from the frequency of a self-modulated proton bunch.

II. EXPERIMENTAL OVERVIEW

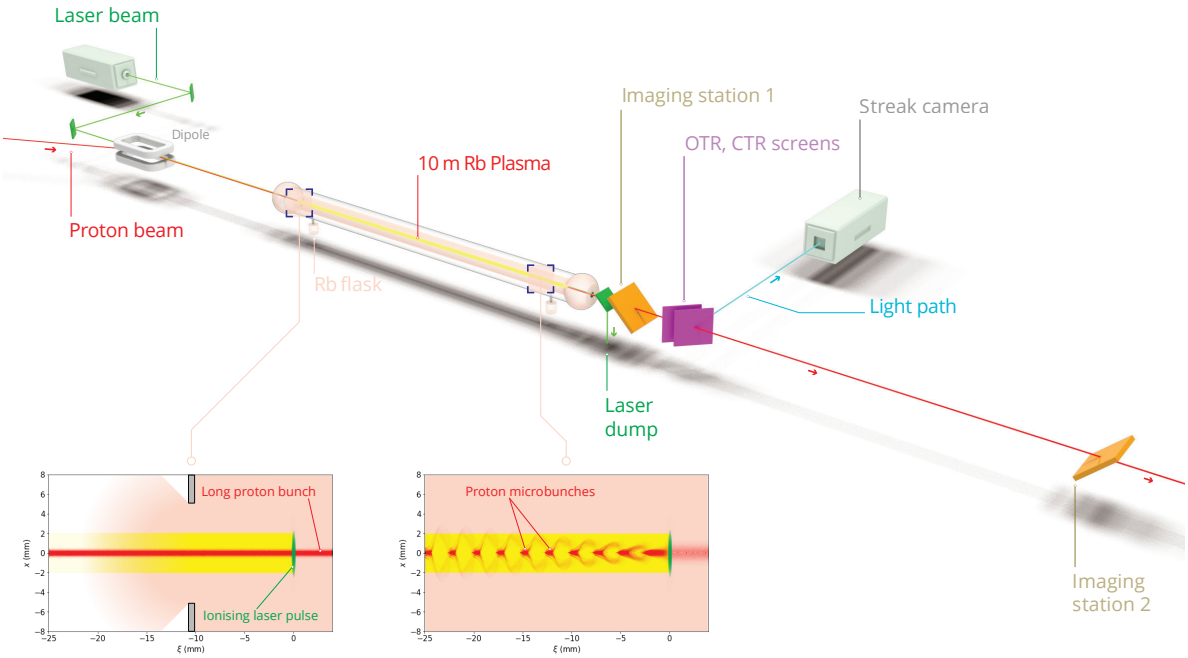

FIG. 1. Experimental layout of the AWAKE experiment showing key components. Dipole magnets and optical mirrors are used to align the proton and laser beams upstream of the vapor cell. Downstream of the cell, the proton beam passes through an OTR foil and optical light is generated in the process. The light is transported to a streak camera for temporal imaging. The inset illustrates a uniform, gaussian proton bunch entering the plasma which is micro-bunched by the time it exits the plasma.

The 400 GeV proton beam from the SPS is delivered to the AWAKE experiment via an 800 m beamline. For the dataset considered here, the proton beam contained $3.03 \pm 0.16 \times 10^{11}$ particles per bunch and a bunch length $\sigma_z = 8.24 \pm 0.15$ cm ($\sigma_t = 275 \pm 5$ ps). The transverse emittance was approximately 3.5 mm·mrad in both planes. The beam is focused to a transverse spot size $\sigma_r \approx 200$ μm at the entrance of the vapor cell. A sketch of the experimental layout highlighting the key components is shown in Figure 1.

The core of the AWAKE experiment is the 10 meter long Rb vapor cell [17, 18]. Rb vapor flows into the cell from reservoirs at either end of the chamber. The heating of Rb reservoirs is adjusted until the vapor density is the same at both ends of the cell. The uniform heating of the cell implies that if the density is the same at both ends, it is uniform throughout. There are diagnostic ports at both ends of the cell where a white-light laser passes through the vapor. The density of the vapor is inferred from spectroscopic measurements of white-light absorption at the 780 nm and 795 nm absorption lines, with an uncertainty of 0.5% [19, 20]. The temperature of the cell was held at 468 K for this measurement.

The Rb vapor is ionized by a terawatt-class Ti:sapphire laser. The laser pulse energy can be varied from 40 to 450 mJ and the pulse length is approximately 120 fs [21]. The laser is focused into the vapor cell with a Rayleigh length of 15 m, resulting in a laser spot size of 2 mm over the entire length of the cell, much larger than the 200 μm proton beam spot size. The main laser pulse is derived from an 88 MHz oscillator. The oscillator phase is locked to the RF phase of the cavities in the SPS ring. This allows for synchronization of the amplified laser pulse with the extracted proton beam with picosecond accuracy.

The principle diagnostic for the measurements described in this paper is a streak camera. The proton bunch passes through a metallic foil two meters downstream of the exit of the Rb cell. The beam produces optical transition radiation (OTR) as it passes through the foil, and the OTR light has the same spatio-temporal pattern as the micro-bunched beam. The light is sent via an optical transport system to a dark room where it is imaged onto the aperture of a streak camera. Inside the streak camera, the OTR photons are converted into electrons by a photocathode and accelerated through a "streak tube" towards a phosphor screen [22]. A time-varying, transverse voltage is applied to the streak tube such that the electrons receive a kick that depends on when they were produced at the photocathode. The electrons arrive at different transverse positions on the phosphor screen and the emitted light is imaged onto a CMOS camera. The streak camera manufacturer provides a calibration

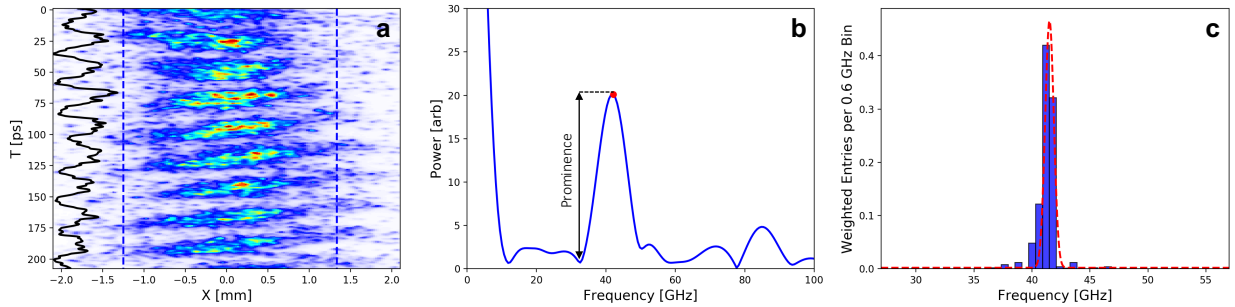

FIG. 2. a) Streak camera image of a modulated proton beam in a 200 ps-long time window. The vertical axis is the time axis, with $t = 0$ denoting the start of the window and not necessarily the start of the proton bunch. The horizontal axis is the transverse spatial coordinate with $x = 0$ located at the beam centroid. The ROI is denoted by dashed blue lines. The solid black line shows temporal projection of the image data in the region of interest. b) The absolute value of the FFT of the projection shown in a) after application of the analysis procedure described in Section III A. A peak in the spectrum is identified at 42.09 GHz using the peak-prominence algorithm and is denoted by the red circle. The prominence is denoted by the black arrow. c) Histogram of the peak frequencies identified with the column-by-column analysis technique. The entries to the histogram are weighted by their prominence and the histogram is fit with a gaussian centered at 41.57 ± 0.07 GHz, where the error on the centroid is extracted from the fit.

of the streak axis so that the vertical dimension of the image is mapped to the co-moving temporal dimension of the beam. The AWAKE streak camera is a Hamamatsu C10910-05 model with a 16-bit, 2048×2048 pixel ORCA-Flash4.0 CMOS sensor, binned to 512×512 pixels for streak operation. The streak camera provides time windows ranging from several ns down to 73 ps. For the smallest time window, the resolution is limited by the streak dynamics rather than the pixel size and is 1 ps [23]. An optical target (Ronchi ruling with 5 lines per mm) was placed at the location of the foil and imaged by the streak camera to determine the point spread function (PSF) in the non-streaked (transverse) plane. The full-width half-maximum (FWHM) resolution in the transverse plane was determined to be 0.187 mm, or roughly 8 pixels.

III. STREAK IMAGE ANALYSIS AND FREQUENCY IDENTIFICATION

The streak camera was operated with a time window of 208 ps near the center of the proton bunch. The streak camera records images of the modulated bunch which are then analyzed to extract the frequency of modulation.

A. Fast Fourier Transform of the Projection

The first step of the analysis to identify the signal region in the streak camera image and take a projection of the data in the region of interest (ROI) along the time axis. A Hann Filter is applied to the projection which is then embedded in a zero-padded array. A Fast Fourier Transform (FFT) is taken of the zero-padded array. The purpose of zero-padding the array is to smooth the result of the FFT, while the Hann Filter prevents aliasing due to embedding. Figures 2a) and 2b) illustrate the signal identification and resulting FFT for a sample image. The modulation frequency is identified by a peak-prominence algorithm. The peak-prominence is defined as the amplitude of the local maximum with respect to the nearest local minimum on the low frequency side of the maximum. This definition reduces sensitivity to the high-amplitude DC component in the signal.

B. Statistical Approach

The FFT of the projection identifies the frequency of modulation averaged transversely across the bunch, since the projection itself is a transverse average across the bunch. It is possible that multiple frequencies appear in a single image, or that the same frequency appears with a phase offset across the image. This is what is observed in the SSM phenomenon, where focused protons appear at the center of the image and defocused protons appear at the edge of the image, phase shifted by 180 degrees [14]. In this case, the projection averages both modulations together out of phase, and the result is a reduced amplitude of the peak frequency.

In order to account for the variation in frequency across the image, the image is subdivided into 40 columns, each 8 pixels wide, corresponding to the FWHM PSF resolution. The FFT is taken for each column and the peak frequency is identified using the peak-prominence algorithm described above. The identified frequencies are added to a histogram, weighted

by their prominence. Finally, a gaussian is fitted to the resulting histogram and the mean peak frequency is determined from the centroid of the fit. The error on the mean is extracted from the covariance matrix of the fit.

The column-by-column analysis has two advantages over the projection approach described in Section III A. First, the algorithm is robust to noise when identifying the peak frequencies in the signal region. Second, it produces a statistical error for each image, which is a measure of our confidence in the signal identification. For the sample data shown in Figure 2, the two approaches produce similar values, where the projection approach gives a value of 42.09 GHz and the column-by-column approach yields 41.57 ± 0.07 GHz.

IV. RESULTS

We study the evolution of the plasma density as a function of time after ionization at three laser pulse energies. The Rb vapor density is held at a constant value of $1.81 \pm 0.09 \times 10^{14}$ cm^{-3}, throughout the measurement. The relative laser–proton timing is adjusted via the phase-locking system described in Section II. The time delay Δt is varied from 0 μs (corresponding to the laser seed pulse coincident with the center of the proton beam) to 80 μs. The laser energy is controlled by changing the angle of an attenuating polarizer. For every time delay setting, we record ten shots each for a laser pulse energy of 135 mJ, 95 mJ, and 40 mJ, which we refer to as the high, medium, and low energy settings, respectively. In addition, we record a single laser-off background shot for each setting, for an average of 33 events per time delay. Figure 3 shows example images of the self-modulated proton bunches for different time delays after ionization with the high-power setting.

The images are grouped by time delay and laser energy setting. We apply the projection analysis to each image (Section III A) and extract a first estimate of the peak frequency for each time delay and laser energy. The results of the projection analysis for the high energy laser setting are shown as a waterfall plot in Figure 4. The projection analysis shows a nearly constant modulation frequency over the first 1 ms, followed by rapid decay. Note that the larger time delays are logarithmically spaced. For time delays $\Delta t \geq 5$ μs, a second peak is observed in the FFT spectrum at twice the frequency of the main peak. The second peak may be the result of events that have a transverse hose instability, which appears as a zigzag pattern on the streak camera image with the same frequency as the SMI, or because

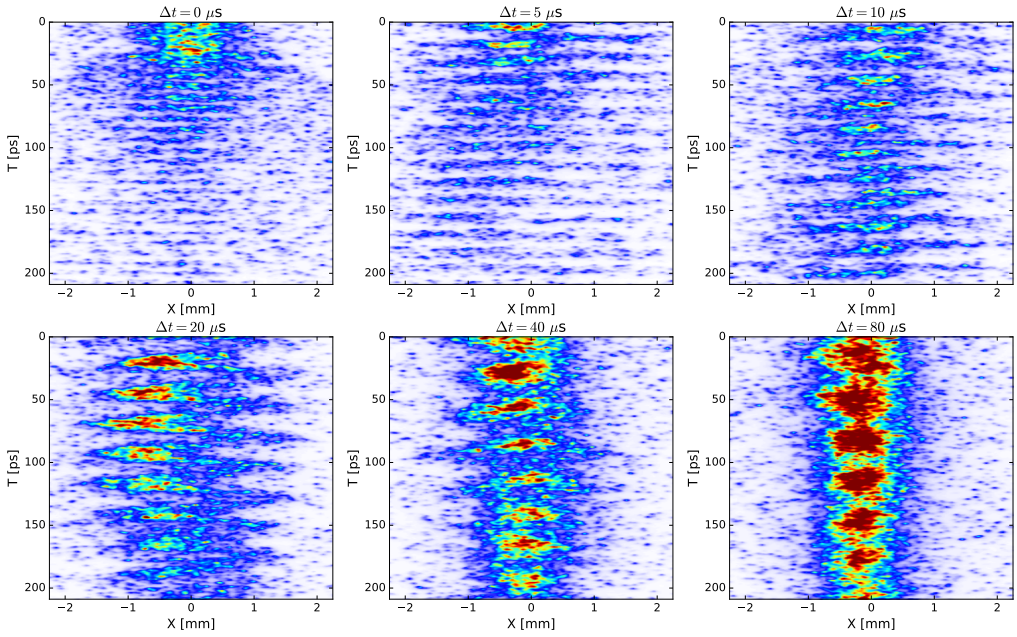

FIG. 3. Streak camera images of the modulated proton beam for example time delays Δt after ionization by the laser pulse with the high-power setting. The images share the same spatial, temporal, and color scales. The frequency of the modulation is clearly observed to be decreasing with time after ionization, indicating a decay in the plasma density. The image at a time delay of 20 μs has the signature of the hose instability which may arise in the case of un-seeded self-modulation.

of harmonics in the SSM signal.

The peak frequencies and error on the frequencies are determined using the statistical analysis described in Section III B. The data points are grouped into sets by time delay and laser pulse energy and the histograms for each image in the set are added together. The fit is performed on the ensemble histogram, with centroids and errors extracted from the fit. Finally, the frequencies ν are converted into plasma densities n with the equation

$$n = \epsilon_0 m_e \left(\frac{2\pi\nu}{e}\right)^2 \tag{1}$$

where ϵ_0 is the permittivity of free space, m_e is the mass of the electron, and e is the charge of the electron. The error on the mean density is given by

$$\sigma_n = 2n\frac{\sigma_\nu}{\nu}, \tag{2}$$

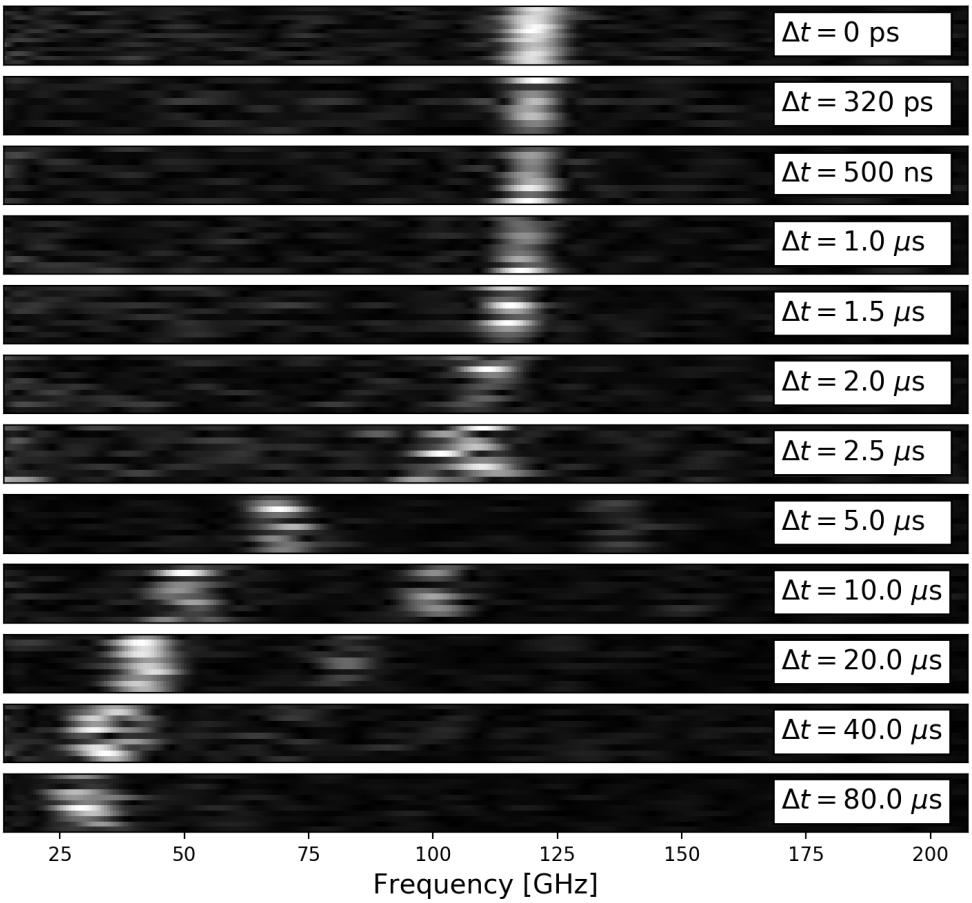

FIG. 4. Waterfall plot of the projected image data for the 135 mJ laser energy setting, with normalized color scale. Each subplot contains approximately 10 stacked Fourier spectra. The subplots are labeled by time after ionization, with 0 s at the top and 80 μs at the bottom. The larger time delays are logarithmically spaced. For time delays $\Delta t \geq 5$ μs, a second peak appears in the spectra at twice the frequency of the main peak. This may be due to the transverse hose instability, or harmonics in the main signal.

where σ_ν is the error on the mean frequency extracted from the gaussian fit of the histogram. Previous work has established that at zero time delay, the correlation between the modulation frequency and the plasma density is exact, and we can conclude that the plasma is fully ionized by the laser [15]. At longer time delays, the connection between the modulation frequency and plasma density is more nuanced, because the plasma may not be uniform across the proton bunch. We interpret the measured modulation frequency as the result of the average plasma density seen by the proton beam.

The results of the time delay scan are shown in Figures 5a) and 5b). Figure 5a) shows the evolution of the plasma density for delays less than 1 μs. The point at $\Delta T = 0$ s has been assigned an offset of 1 ps so that is visible on log x-axis plot. Further, the high, medium, and low energy data points are assigned small temporal offsets so that the error bars are visible without overlap, but all groups of points are taken at the same time delay, namely 0, 320 ps, 500 ns, and 1 μs. The errors are multiplied by a factor of 5 so that they are visible. The measured plasma densities at 0 s, 320 ps, and 500 ns, are close to, but slightly less than the measured vapor density, shown with a 0.5% uncertainty in gray. The discrepancy could result from less than 100% ionization, or systematic error in the frequency measurement, but of particular significance is the fact that the measured density is unchanging over the first 500 ns. A roll-off in density begins to appear around 1 μs after ionization.

Figure 5b) shows the evolution of the plasma density for time delays of 500 ns and longer, plotted on a log-log scale. The low energy data point at $\Delta t = 2.0$ μs has been removed due to noise in the signal. Error bars are plotted but are not visible on the the log-log scale. For time delays 10 μs and greater, the data are fit with a power law of form at^b. The significance of the power law evolution is discussed in Section V.

V. MODEL AND ANALYSIS

The data show two important features which we attempt to model. First, we observe a plateau in the plasma density for delays up to 1 μs. Second, we observe a power law-like decay of the plasma density at long time delays. Our model starts by considering the formation of the plasma column.

A. Plasma Formation

The ionizing laser has a nearly constant spot size of 2 mm throughout the 10 m long vapor cell. The peak intensity of the laser is 9.0×10^{12} W/cm^2, 6.3×10^{12} W/cm^2, 2.6×10^{12} W/cm^2, for the 135 mJ, 95 mJ, and 40 mJ laser energy settings, respectively. The first energy level of Rb is $U = 4.18$ eV, while the Ti:sapphire laser photon energy is $h\nu = 1.59$ eV at a central wavelength of 780 nm. In all cases, the Keldysh parameter

$$\gamma_k = \frac{\omega\sqrt{2m_eU}}{eE} > 1, \tag{3}$$

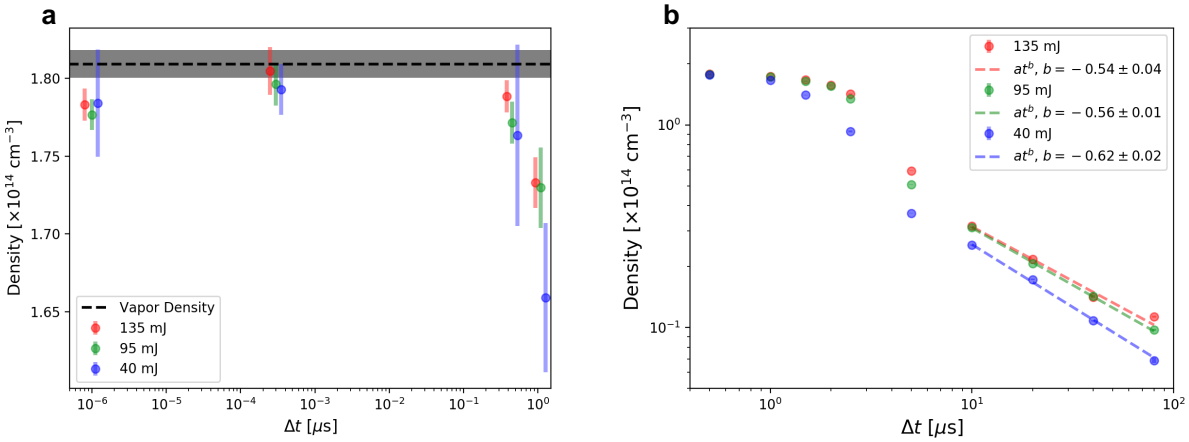

FIG. 5. a) Plasma density versus time after ionization for delays up to 1 μs, for the high, medium, and low energy laser settings, plotted on a log x-axis. The errors are shown multiplied by a factor of five so that they are visible in the plot. The measured vapor density with a 0.5% uncertainty is also shown. The data points corresponding to $\Delta t = 0$ s are assigned an offset of 1 ps so that they are visible in the plot. In addition, the high, medium, and low energy data points are assigned small temporal offsets so that the error bars are visible without overlap, but all groups of points are taken at the same time delay, namely 0, 320 ps, 500 ns, and 1 μs. b) Plasma density versus time after ionization for delays of 500 ns and greater. The data point corresponding to the low energy setting at $\Delta t = 2.0$ μs has been excluded due to noise in the signal. A power law fit of the form at^b is applied to the data for $\Delta t \geq 10$ μs.

where ω is the laser frequency and E is the peak electric field [24]. For $\gamma_k > 1$, the dominant ionization mechanism is multi-photon absorption. We use simulations based on the PPT model to describe the ionization of the Rb vapor by the laser [25]. In particular, we are interested in the spatial distribution and temperature of the ionized electrons, as this will serve as the initial conditions for our plasma evolution model.

Figure 6a) shows the radial and longitudinal ionization fraction of the Rb vapor along the 10 m length of the cell for the 135 mJ laser energy setting. The average radius of ionization is 2.2 mm. The transverse laser profile used in the model was gaussian, but the laser mode profile in the experiment has a top-hat shape. Further simulations were performed with super-gaussian modes. The results of these simulations show less uniformity at the boundary of the ionized region, but produce a similar value for the average ionized

radius. Figure 6b) shows the average energy of the plasma electrons in the ionized region. The minimum energy of ionization is 0.59 eV, corresponding to three-photon absorption $E_{min} = U - 3h\nu$. The median electron energy after ionization is 0.62 eV. The model does not include plasma electron energy gain in the ponderomotive potential of the laser pulse, which has a maximum amplitude of $U_p = 0.51$ eV. We expect the energy contribution from U_p to be negligible given that the laser is linearly polarized and plasma electrons will be preferentially ionized at the maximum of the electric field which corresponds to the zero-crossing of the ponderomotive potential. Simulations were also performed for the 95 mJ and 40 mJ laser energy settings. At 95 mJ, the average ionized radius is 2.0 mm and at 40 mJ it is 1.7 mm. In all cases, the median energy of the plasma electrons after ionization is 0.62 eV.

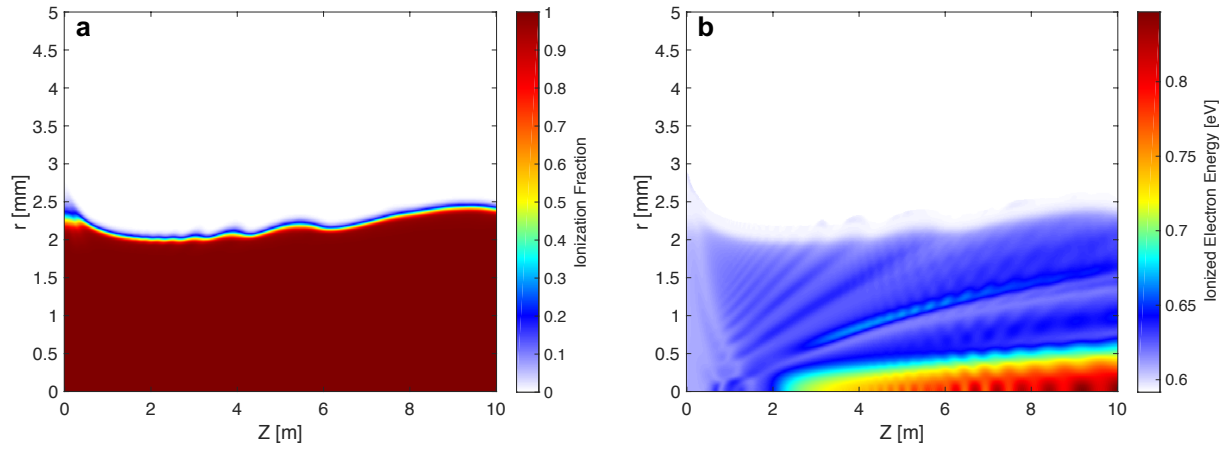

FIG. 6. a) Ionization fraction for the 135 mJ laser pulse setting with a gaussian transverse pulse shape based on the PPT model. The average radius of the ionized plasma column is 2.2 mm. b) Energy of ionized electrons. The minimum energy after ionization is 0.59 eV, while the median energy is 0.62 eV.

B. Thermalization, Diffusion, and Recombination

Several processes contribute to the evolution of the plasma column after ionization. We consider the following three effects in detail: diffusion, thermalization, and recombination. For both diffusion and thermalization, the key parameter of interest is the collision fre-

quency [26]

$$\nu_{\alpha,\beta} = 1.8 \times 10^{-19} \frac{(m_\alpha m_\beta)^{1/2} n \lambda_{\alpha,\beta}}{(m_\alpha T_\beta + m_\beta T_\alpha)^{3/2}}, \tag{4}$$

where m is the particle mass, T is the temperature, n is the density, and λ is the Coulomb logarithm. Here, α and β represent two species in the plasma, so the same equation can be used to calculate the electron-electron collision frequency ν_{ee}, the ion-ion collision frequency ν_{ii}, and the electron-ion collision frequency ν_{ei}. Immediately after ionization, the electron distribution is non-thermal, with a median electron energy of $E_{e0} = 0.62$ eV. The electron thermalization time is $t_{ee} = \nu_{ee}^{-1} \approx 100$ ps. The temperature of the electrons after thermalization is $T_{e0} = 2E_{e0}/3 = 0.41$. The ions are already thermal at the time of ionization with a temperature of $T_{i0} = 0.040$ eV and will come to equilibrium with the electrons in time $t_{ei} = \nu_{ei}^{-1} \approx 7$ μs, which is much longer than the electron thermalization time.

Diffusion describes the expansion of the plasma column into the unionized vapor. The collision frequency determines the ion diffusion rate

$$D_i = \frac{T_i}{m_i \nu_{tot}}, \tag{5}$$

where $\nu_{tot} = \nu_{ii} + \nu_{i0}$ is the sum of the ion-ion collision rate and the ion-neutral collision rate. In the case of a plasma with hot electrons and cold ions, the electrons increase the diffusion rate of the ions such that both species evolve at the ambipolar diffusion rate $D_a \approx D_i(1+T_e/T_i)$ [27]. Inside the column, where there is complete ionization of the plasma, the diffusion rate is dominated by ion-ion collisions ($\nu_{tot} = \nu_{ii}$) and the mean free path is short $l = v_t/\nu_{ii} = 1.75$ μm, where v_t is ion thermal velocity. Outside the plasma column, the mean free path of the ions is determined by ion-neutral collision frequency ($\nu_{tot} = \nu_{i0}$). The ion-neutral charge exchange cross section is given by $\sigma_{Rb} = (a - b \ln v_t)^2$, with $a = 42 \times 10^{-8}$ cm and $b = 1.85 \times 10^{-8}$ cm [28]. For an ion thermal velocity of $v_t = 3.69 \times 10^4$ cm/s, we find $\sigma_{Rb} = 5 \times 10^{-14}$ cm^2, which at a neutral density $n_0 = 1.81 \times 10^{14}$ cm^{-3} yields a mean free path $l = v_t/\nu_{i0} = 1.1$ mm, much larger than the mean free path inside the column. The ambipolar diffusion rate varies greatly between the ionized and unionized regions, jumping from 10 cm^2/s to 15,000 cm^2/s across the boundary of the plasma column. In this scenario, the expansion of the plasma column into the unionized vapor is described by the time-dependent ambipolar diffusion wave equation [29]

$$\frac{1}{v_a^2} \frac{\partial^2 n}{\partial t^2} + \frac{1}{D_a} \frac{\partial n}{\partial t} = \nabla n, \tag{6}$$

where $v_a = (\gamma_r T_e/m_i)^{1/2}$ is the ambipolar velocity, with γ_r the ratio of the specific heats of the plasma and vapor. For times $t < D_a/v_a^2 = 1.5$ μs, we neglect the diffusion term and the expansion of the plasma column is described by a wavefront propagating into the neutral vapor at speed $v_a \approx 9.6 \times 10^4$ cm/s, with $\gamma_r = 2$ for hot plasma diffusing into neutral gas following the convention used in Reference [30]. While the edge of the column expands outwards, a density depression propagates inwards, etching away at the plasma column. The on-axis density remains constant until the inward propagating wave reaches the axis, at which point it starts to drop rapidly.

Equation 6 is evaluated numerically for different electron temperatures T_e and plasma column radii r_0 and compared with the data. Assuming an initial electron temperature of 0.41 eV, and an initial plasma density $n_0 = 1.785 \times 10^{14}$ cm^{-3}, corresponding to the average measured plasma density at $\Delta t = 0$, we fit the model to the data and find the initial plasma radii to be 1.73 mm, 1.70 mm, and 1.63 mm for the high, medium, and low energy laser settings, respectively. On the other hand, higher electron temperatures are consistent with larger initial radii, and vice versa, because the two quantities can be combined to produce the same etching time of the plasma column $t_{etch} = r_0/v_a$. Figure 7 shows the data in the range $0.5 \leq \Delta t \leq 1.5$ μs compared to the on-axis density curves from the model. The dashed lines indicate the fit to the data at a fixed temperature of 0.41 eV, while varying the initial plasma radius. Note that the model cannot simultaneously provide a good fit to the data at $\Delta t = 1.0$ and $\Delta t = 1.5$ μs. We also show a gray region corresponding to other model parameters consistent with the data. These parameters include initial plasma electron temperatures in the range of $0.39 \leq T_e \leq 0.73$ eV. The lower limit corresponds to the case where electrons are ionized with the minimal possible energy (3-photon absorption), while the upper limit corresponds to the case where the electrons gain an additional 0.51 eV of energy in the ponderomotive potential of the laser. As discussed in Section V A, we expect the energy gain from the ponderomotive potential to be small, and therefore the upper bound chosen for the electron temperature is a conservative estimate. The initial plasma column radii that are consistent with the data in the range of temperatures cited above is $r_0 = 1.58$ mm at $T_e = 0.39$ eV and $r_0 = 2.30$ mm at $T_e = 0.73$ eV. In future experiments, we will make an independent measurement of the initial plasma radius via Schlieren imaging and this information can be used to break the degeneracy of the model.

For times delays between $1.5 \leq \Delta t \leq 10$ μs, the dominant processes are diffusion and

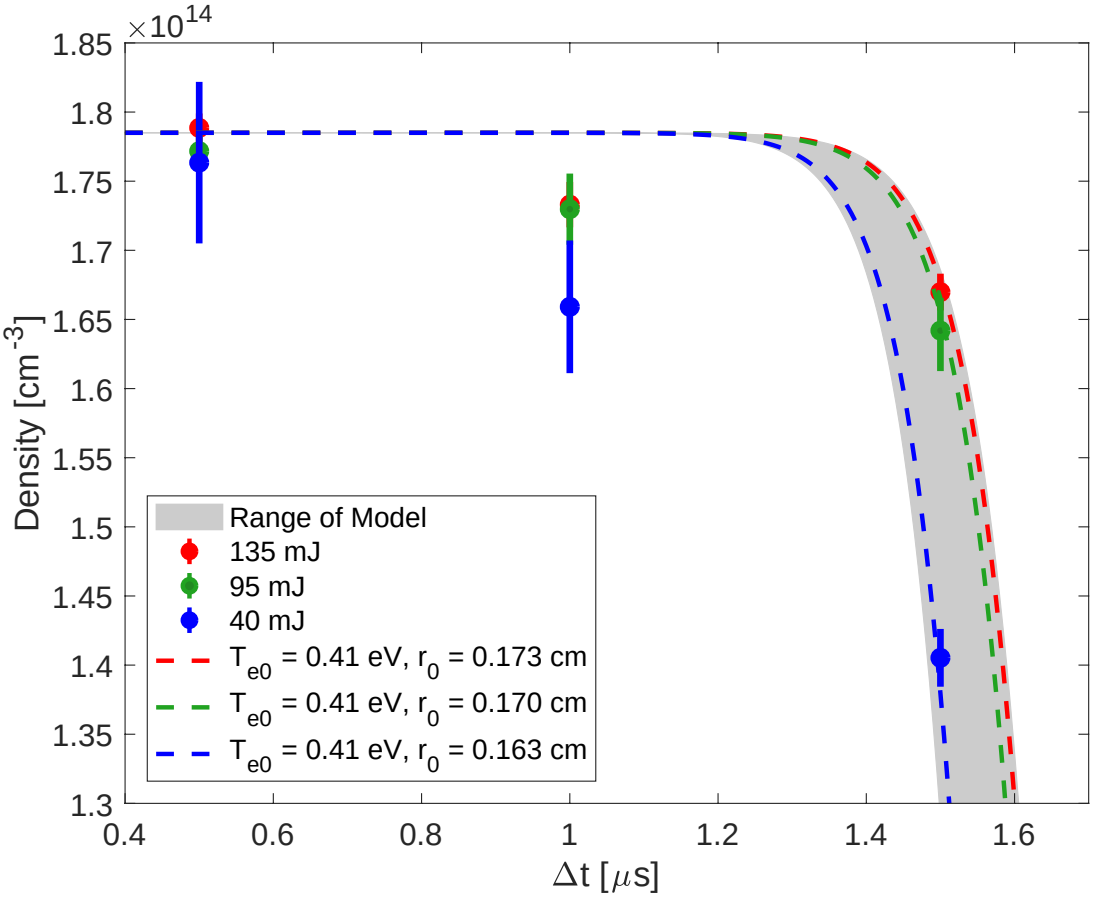

FIG. 7. Plasma density versus time compared to the on-axis density curves from the model. The red, blue and green data points correspond to the high, medium, and low energy laser settings, respectively, shown with error bars multiplied by five. The dashed lines are fits to the data at a fixed initial electron temperature of 0.41 eV. The shaded gray region shows the region of degeneracy of the model, where different values of T_e and r_0 produce similar on-axis density curves, so long as $t_{etch} = r_0/v_a \approx 1.5$ μs.

thermalization. During this time, the plasma spreads out and cools as the electrons come to equilibrium with the ions. The cool electrons may then start to recombine with the ions through the 3-body recombination process

$$\frac{dn}{dt} = -\alpha_3 n^3, \tag{7}$$

with α_3 given by [26]

$$\alpha_3 = 8.75 \times 10^{-27} T_e^{-4.5}. \tag{8}$$

The strong dependence on temperature in equation 8 explains why no recombination occurs until the electrons are cooled by coming to equilibrium with the ions. After thermalization, α_3 is constant and Equation 7 has solution

$$n(t) = \left(2\alpha_3 t + n_0^{-2}\right)^{-1/2}. \tag{9}$$

Figure 5b) shows the data at times $10 \leq \Delta t$ μs fit with a power law. The extracted powers are close to but slightly more negative than -0.5. It is likely that there are other plasma loss mechanisms at extremely long time delays, such as plasma reaching the wall of the cell, which contribute to a higher rate of decay of the plasma density.

VI. DISCUSSION AND SUMMARY

In this work, we measure the decay of a singly-ionized Rubidium plasma for times after ionization $0 < \Delta t < 80$ μs. The plasma density is inferred from the frequency of modulation of a high energy proton beam. We observe two features in the data: a plateau in the plasma density for times $\Delta t \lesssim 1$ μs, and a power law decay for 10 μs $\lesssim \Delta t$. The short-time delay behavior is modeled using the time-dependent ambipolar diffusion wave equation, while the long-time delay behavior is described by 3-body recombination.

This measurement was motivated by interest in the self-modulation instability and optimal conditions for proton beam-driven plasma wakefield. We find that it is indeed important to suppress ionization prior to the transit of the proton beam driver in order to control the seeding of the wakefield. Possible sources of ionization include laser pre-pulses or impact ionization by the head of the proton driver. The latter source is intrinsic to the physics of SSM. Therefore, the plasma density arising from impact ionization can be considered the background plasma density that the system should return to prior to the passage of a subsequent bunch. For a vapor density of 1.81×10^{14} cm^{-3}, we extrapolate the results of Reference [31] to estimate a background density of $4 - 8 \times 10^{11}$ cm^{-3}. Extrapolating from the fit presented in Figure 5b), we find that it takes approximately 25 ms after ionization to reach this density. This time scale is short compared to the 20 second repetition rate of the AWAKE experiment, but long compared to the repetition rate of other accelerators used in high-energy physics applications, which often operate with sub-microsecond bunch spacing.

This work considers the decay of a cold plasma after ionization by a laser pulse, but

there will be an additional contribution to the plasma electron energy from the passage of previous proton beams driving large amplitude wakefields. In this case the plasma electron energy will be in the keV range and the subsequent thermalization and recombination will require even more time. In future experiments, we aim to probe this effect by sending two proton beams through the vapor cell and measuring the effect of the leading on bunch on the trailing bunch as a function of the separation between the beams.

---

[1] R. Assmann *et al.* (AWAKE Collaboration), Plasma Phys. Control. Fusion **56**, 084013 (2014), arXiv:1401.4823 [physics.acc-ph].

[2] A. Caldwell *et al.* (AWAKE Collaboration), Nucl. Instrum. Meth. **A829**, 3 (2016), arXiv:1511.09032 [physics.plasm-ph].

[3] E. Gschwendtner *et al.* (AWAKE Collaboration), Nucl. Instrum. Meth. **A829**, 76 (2016), arXiv:1512.05498 [physics.acc-ph].

[4] P. Muggli *et al.* (AWAKE Collaboration), Plasma Phys. Control. Fusion **60**, 014046 (2017), arXiv:1708.01087 [physics.plasm-ph].

[5] M. Litos *et al.*, Nature **515**, 92 (2014).

[6] W. P. Leemans *et al.*, Phys. Rev. Lett. **113**, 245002 (2014).

[7] A. Caldwell *et al.*, Nature Phys. **5**, 363 (2009), arXiv:0807.4599 [physics.acc-ph].

[8] E. Adli, J.-P. Delahaye, S. J. Gessner, M. J. Hogan, T. Raubenheimer, W. An, C. Joshi, and W. Mori, in *Proceedings, 2013 Community Summer Study on the Future of U.S. Particle Physics: Snowmass on the Mississippi (CSS2013): Minneapolis, USA, 2013* (2013) arXiv:1308.1145 [physics.acc-ph].

[9] C. B. Schroeder, E. Esarey, C. G. R. Geddes, C. Benedetti, and W. P. Leemans, Phys. Rev. ST Accel. Beams **13**, 101301 (2010).

[10] N. Kumar *et al.*, Phys. Rev. Lett. **104**, 255003 (2010).

[11] C. B. Schroeder *et al.*, Phys. Rev. Lett. **107**, 145002 (2011).

[12] A. Pukhov *et al.*, Phys. Rev. Lett. **107**, 145003 (2011).

[13] K. V. Lotov, Physics of Plasmas **22**, 103110 (2015), https://doi.org/10.1063/1.4933129.

[14] M. Turner *et al.* (AWAKE Collaboration), Phys. Rev. Lett. **122**, 054801 (2019).

[15] E. Adli *et al.* (AWAKE Collaboration), Phys. Rev. Lett. **122**, 054802 (2019).

[16] J. Vieira *et al.*, Phys. Rev. Lett. **112**, 205001 (2014).

[17] G. Plyushchev *et al.*, J. Phys. D: Appl. Phys **51** (2018).

[18] E. Öz *et al.*, Nucl. Instrum. Meth. **A740**, 197 (2014).

[19] E. Öz *et al.*, Nucl. Instrum. Meth. **A829**, 321 (2016), arXiv:1511.08763 [physics.ins-det].

[20] F. Batsch, M. Martyanov, E. Oez, J. Moody, E. Gschwendtner, A. Caldwell, and P. Muggli, Nuclear Instruments and Methods in Physics Research Section A: Accelerators, Spectrometers, Detectors and Associated Equipment **909**, 359 (2018), 3rd European Advanced Accelerator Concepts workshop (EAAC2017).

[21] V. Fedosseev *et al.*, in *Proceedings of the 7th International Particle Accelerator Conference (IPAC): Busan, Korea, May 2016*, pp. 2592 – 2595.

[22] Hamamatsu, *Guide to Streak Cameras* (Hamamatsu Corporation, 2008).

[23] K. Rieger *et al.*, Review of Scientific Instruments **88**, 025110 (2017), https://doi.org/10.1063/1.4975380.

[24] L. V. Keldysh, Soviet Physics JETP **20**, 1307 (1965).

[25] A. Perelomov, V. Popov, and M. Terentev, Soviet Physics JETP **23**, 924 (1966).

[26] J. D. Huda, *NRL Plasma Formulary* (Office of Naval Research, 2016).

[27] F. F. Chen, *Introduction to Plasma Physics and Controlled Fusion* (Springer, 2016).

[28] J. Perel, R. H. Vernon, and H. L. Daley, Phys. Rev. **138**, A937 (1965).

[29] Z. Shimony and J. H. Cahn, Physics of Fluids **8**, 1704 (1965).

[30] J. Hyman, Journal of Applied Physics **39**, 4568 (1968).

[31] G. Fior, *Study of impact ionization by a proton bunch*, Master's thesis, TU Munich (2017).